

Second-Order Møller–Plesset Perturbation Theory in the Condensed Phase: An Efficient and Massively Parallel Gaussian and Plane Waves Approach

Mauro Del Ben,^{*,†} Jürg Hutter,^{*,†} and Joost VandeVondele^{*,‡}

[†]Institute of Physical Chemistry, University of Zürich, Winterthurerstrasse 190, CH-8057 Zürich, Switzerland

[‡]Department of Materials, ETH Zürich, Wolfgang-Pauli-Strasse 27, CH-8093 Zürich, Switzerland

S Supporting Information

ABSTRACT: A novel algorithm, based on a hybrid Gaussian and plane waves (GPW) approach, is developed for the canonical second-order Møller–Plesset perturbation energy (MP2) of finite and extended systems. The key aspect of the method is that the electron repulsion integrals ($ial\lambda\sigma$) are computed by direct integration between the products of Gaussian basis functions $\lambda\sigma$ and the electrostatic potential arising from a given occupied-virtual pair density ia . The electrostatic potential is obtained in a plane waves basis set after solving the Poisson equation in Fourier space. In particular, for condensed phase systems, this scheme is highly efficient. Furthermore, our implementation has low memory requirements and displays excellent parallel scalability up to 100 000 processes. In this way, canonical MP2 calculations for condensed phase systems containing hundreds of atoms or more than 5000 basis functions can be performed within minutes, while systems up to 1000 atoms and 10 000 basis functions remain feasible. Solid LiH has been employed as a benchmark to study basis set and system size convergence. Lattice constants and cohesive energies of various molecular crystals have been studied with MP2 and double-hybrid functionals.

1. INTRODUCTION

The second-order Møller–Plesset (MP2) energy is an effective correction to the Hartree–Fock ground state energy that accounts for electron correlation effects. It is obtained from Rayleigh–Schrödinger perturbation theory, for which the zeroth-order Hamiltonian is chosen as the sum of the one-electron Fock operators.^{1,2} MP2 is appealing because it recovers a relatively large part of the dynamic correlation and maintains an easy and compact formulation. Most notably, MP2 introduces dispersion, which is an essential noncovalent interaction. Furthermore, MP2 is also available for condensed phase systems, i.e., including periodic boundary conditions.^{3–9} With the introduction of double-hybrid density functionals,^{10,11} MP2-like correlation has also established itself in density functional theory (DFT). In double hybrids, an MP2-like term obtained from the Kohn–Sham orbitals and eigenvalues is mixed into the correlation energy. However, the advantages of MP2 come at a computational cost that is high compared to that of Hartree–Fock or traditional DFT. In its canonical formulation, MP2 scales as $O(n^5)$, where n represents the number of basis functions, and a large amount of memory is needed to store the intermediates of the calculation. Furthermore, MP2 calculations need larger basis sets than DFT to reach a similar convergence. In order to extend the applicability of MP2 to large systems these limitations have to be overcome.¹²

Various reformulations of the MP2 energy expression and new algorithms have been proposed to address these limitations. Reducing the formal $O(n^5)$ scaling is achieved with methods such as local MP2^{7,13–21} (LMP2) and Laplace-transformed MP2.^{6,22–27} The prefactor of the various terms

that dominate for smaller systems can be reduced with the resolution of identity approximation^{4,5,28–33} (RI-MP2), while explicitly correlated methods speed up the convergence of the MP2 energy with respect to basis set size³⁴ (F12-MP2). Despite this progress, calculations with good basis sets on systems containing 50 or more heavy atoms remain computationally demanding with MP2 or double-hybrid DFT. In order to perform such calculations with acceptable time to solution, massively parallel computing is an indispensable tool. A variety of MP2 algorithms suitable for parallel architectures has been proposed,^{35–45} and these algorithms have demonstrated good scalability up to a few hundred cores.

Here, we present a novel MP2 algorithm that is particularly suitable for the condensed phase and has been designed to achieve excellent scalability on modern massively parallel architectures having thousands to hundreds of thousands of cores. The prefactor of the $O(n^5)$ term is minimal, and the memory usage per core is small. It is based on the Gaussian and plane wave (GPW) approach,⁴⁶ which allows for avoiding computation of four center electron repulsion integrals (ERI) over Gaussian basis functions ($\mu\nu\lambda\sigma$). In conventional canonical MP2 algorithms, computation of these integrals and their transformation into the molecular orbital basis is usually the most time-consuming step. This step is furthermore difficult to parallelize efficiently, involving significant communication and difficult load balancing issues. In the Gaussian and plane wave MP2 (GPW-MP2) method, half-transformed ERIs of the type ($ial\lambda\sigma$) are directly computed in a communication-

Received: June 25, 2012

Published: September 4, 2012



free way. This is achieved by direct computation of the electrostatic potential of the pair density $\rho^{ia} = \psi_i \psi_a$ in an auxiliary plane waves basis by means of fast Fourier transforms (FFTs) and numerical integration of this potential in real space over products of pairs of Gaussian basis functions $\lambda\sigma$. With this strategy, only fully transformed ERIs ($ialjb$) are communicated for calculation of the exchange-like part of the MP2 energy. The efficiency derives from the use of regular auxiliary grids and FFTs, which distinguishes the method from other approaches employing numerical integration.^{47,48} We report parallel scalability up to 100 000 processes with 80% efficiency, allowing calculations on molecular crystals containing more than 5000 basis functions within minutes. We further validate the GPW-MP2 method by performing calculations on molecular crystals with extended basis sets.

2. GAUSSIAN AND PLANE WAVE MP2 METHOD

In the canonical orbital formalism, the closed-shell MP2 correlation energy $E^{(2)}$ is obtained as

$$E^{(2)} = - \sum_{ij,ab}^{\text{occ,vir}} \frac{(ialjb)[2(ialjb) - (iblja)]}{\epsilon_a + \epsilon_b - \epsilon_i - \epsilon_j} \quad (1)$$

Indices ij refer to occupied and a,b to virtual canonical orbitals and ϵ_p to the corresponding orbital energy. The ERIs over molecular orbitals (MO ERI) are given by

$$(ialjb) = \iint \psi_i(\vec{r}_1) \psi_a(\vec{r}_1) \frac{1}{r_{12}} \psi_j(\vec{r}_2) \psi_b(\vec{r}_2) d\vec{r}_1 d\vec{r}_2 \quad (2)$$

and conventionally computed by a four-index transformation from ERIs over atomic orbitals (AO ERI) ($\mu\nu\lambda\sigma$) as

$$(ialjb) = \sum_{\mu\nu\lambda\sigma} (\mu\nu\lambda\sigma) C_{\mu i} C_{\nu a} C_{\lambda j} C_{\sigma b} \quad (3)$$

where $C_{\mu i}$ represent elements of the MOs coefficient matrix and Greek indices refer to AOs, a linear combination of Gaussian basis functions in our approach. For systems described by periodic boundary conditions (PBC), Brillouin sampling is implicitly implied for eq 1, but here we will assume that Γ -point sampling is sufficient for systems with a sufficiently large unit cell and band gap.^{3,8,49} In the periodic case, AOs and the integrals in eq 2 must take the PBC into account.⁴⁶

The basis of the Gaussian and plane wave MP2 method (GPW-MP2) is the direct formulation of the half-transformed ERIs based on the electrostatic potential v^{ia} of the pair density ρ^{ia}

$$\begin{aligned} (ial\lambda\sigma) &= \iint \psi_i(\vec{r}_1) \psi_a(\vec{r}_1) \frac{1}{r_{12}} \phi_\lambda(\vec{r}_2) \phi_\sigma(\vec{r}_2) d\vec{r}_1 d\vec{r}_2 \\ &= \int \left[\int \frac{\rho^{ia}(\vec{r}_1)}{r_{12}} d\vec{r}_1 \right] \phi_\lambda(\vec{r}_2) \phi_\sigma(\vec{r}_2) d\vec{r}_2 \\ &= \int v^{ia}(\vec{r}_2) \phi_\lambda(\vec{r}_2) \phi_\sigma(\vec{r}_2) d\vec{r}_2 \end{aligned} \quad (4)$$

The form of the last equation is essentially identical to the one used in the GPW method⁴⁶ to compute matrix elements of the Hartree potential. Thus, the highly efficient implementation of that operation in CP2K⁵⁰ can be directly used, and we refer to ref 51 for a detailed discussion.

Central in the GPW method is the representation of the density $\rho^{ia}(\vec{r})$ on a regular grid, which can be considered

equivalent to an expansion of the density in an auxiliary basis of plane waves (PW). The expansion is given by

$$\rho^{ia}(\vec{r}) \approx \frac{1}{\Omega} \sum_{|\vec{G}| \leq G_c} \rho^{ia}(\vec{G}) e^{i\vec{G} \cdot \vec{r}} \quad (5)$$

where the sum over the reciprocal lattice vectors \vec{G} is determined by the resolution of the grid. $\rho^{ia}(\vec{G})$ are the Fourier coefficients of the density, and Ω is the volume of the simulation cell. Conventionally, the resolution of the grid is specified as the energy cutoff $(1/2)G_c^2$ that limits the kinetic energy of the PWs. Fast Fourier transforms (FFTs) efficiently change representation between real space ($\rho^{ia}(\vec{R})$) and reciprocal space ($\rho^{ia}(\vec{G})$). In particular, for a grid with S grid points, the transformation can be performed in linear scaling time ($O(S \log S)$). In reciprocal space, it becomes straightforward to solve the Poisson equation for the potential v^{ia}

$$v^{ia}(\vec{G}) = \frac{4\pi}{G^2} \rho^{ia}(\vec{G}) \quad (6)$$

and an additional back FFT (FFT^{-1}) will yield the potential in real space. The orthonormality of the orbitals implies that $\rho^{ia}(\vec{G} = 0) = 0$, and divergence at $\vec{G} = 0$ is thus avoided.⁵² Note that the PW auxiliary basis is a natural choice for periodic systems, but it can equally be used for gas-phase or surface calculations. Indeed, once the density is specified on a regular grid efficient methods are available for solving the Poisson equation with free (for example cluster or slab) boundary conditions.^{53–55} The simplicity of the GPW method has as a drawback that all-electron calculations are not possible and that pseudopotentials have to be employed in order to have densities that are smooth. The Gaussian and augmented plane wave (GAPW) scheme^{56,57} overcomes this limitation and is suitable for all-electron calculations. However, whereas this method is available in CP2K for all-electron DFT calculations, our MP2 implementation is currently limited to the GPW method only.

Once the potential v^{ia} is available on a regular real space grid, numerical integration over the basis functions is performed by summing the product of the value of the potential and the primitive Gaussian functions (PGFs) over the grid points. Within a given threshold (ϵ_{grid}), all nonzero matrix elements for a given pair ia can be obtained in linear scaling time. This is possible since only pairs of overlapping Gaussians need to be considered, and only a finite number of grid points within a spherical region around the center of the PGF is required. A further gain in efficiency is obtained by employing a multigrid technique that represents the potential v^{ia} on grids with increasingly coarser grid spacing. Depending on the smoothness or width of the PGF, the appropriate grid is selected so that the number of points employed for integration is essentially independent of the exponent of the PGF. The accuracy of the multigrid scheme is fixed by specifying a relative cutoff ($E_{\text{cut}}^{\text{rel}}$) that specifies the E_{cut} of the grid that will be employed for a PGF with exponent 1.0.

Finally, ($ial\lambda\sigma$) integrals are transformed into MO ERIs using sparse matrix multiplication. Introducing for a given pair ia the matrix of half-transformed ERIs \mathbf{B}^{ia} ($(ial\lambda\sigma) = B_{\lambda\sigma}^{ia}$), the matrix of MO ERIs \mathbf{V}^{ia} is obtained by two index transformations as $\mathbf{V}^{ia} = \mathbf{C}_o^\dagger \mathbf{B}^{ia} \mathbf{C}_v$, where \mathbf{C}_o and \mathbf{C}_v represent the coefficient matrices of the occupied and virtual orbitals. Multiplication by \mathbf{C}_v can exploit the sparsity of \mathbf{B}^{ia} , implying an $O(nv)$ scaling per ia pair, while the final multiplication cannot

exploit sparsity and is asymptotically dominant, scaling as $O(ovn)$. o , v , and n refer to the number of occupied, virtual, and total orbitals, respectively. The thresholding in the sparse matrix multiplication is enforced using a threshold $\varepsilon_{\text{filter}} \approx \varepsilon_{\text{grid}}$. As we will show below, the overall accuracy of the MP2 energy can be well controlled and for the systems tested here is on the order of 10^{-7} – 10^{-8} au per heavy atom for $E_{\text{cut}} = 300$ Ry, $E_{\text{cut}}^{\text{rel}} = 50$ Ry, $\varepsilon_{\text{filter}} = \varepsilon_{\text{grid}} = 10^{-8}$. E_{cut} depends on the largest exponent of the basis used, while the other parameters are system independent.

3. IMPLEMENTATION OF THE GAUSSIAN AND PLANE WAVE MP2 METHOD

3.1. Serial Algorithm. The pseudocode for the serial algorithm is presented in Figure 1. In a first step, the wave

Loop over all i occupied orbitals

Calculate wavefunction $\psi_i(\vec{R})$ on the real space grid

Store $\psi_i(\vec{R})$

End i Loop

Loop over all a virtual orbitals

Calculate wavefunction $\psi_a(\vec{R})$ on the real space grid

Loop over all i occupied orbitals

Compute $\rho^{ia}(\vec{R}) = \psi_i(\vec{R}) * \psi_a(\vec{R})$ on the real space grid

Transfer $\rho^{ia}(\vec{R}) \rightarrow \rho^{ia}(\vec{G})$: $\rho^{ia}(\vec{G}) = \text{FFT}[\rho^{ia}(\vec{R})]$

Solve the Poisson equation: $\rho^{ia}(\vec{G}) \rightarrow v^{ia}(\vec{G})$

Transfer $v^{ia}(\vec{G}) \rightarrow v^{ia}(\vec{R})$: $v^{ia}(\vec{R}) = \text{FFT}^{-1}[v^{ia}(\vec{G})]$

Integrate potential in real space: $(ia|\lambda\sigma) = B_{\lambda\sigma}^{ia} = \int v^{ia}(\vec{R}) \phi_{\lambda}(\vec{R}) \phi_{\sigma}(\vec{R}) d\vec{R}$

Index transformations $V^{ia} = C_o^{\dagger} (B^{ia} C_v)$

Store V^{ia}

End i Loop

$$E^{(2)} = E^{(2)} + \sum_{ij,b} \frac{(ia|jb)[2(ia|jb) - (ja|ib)]}{\varepsilon_i + \varepsilon_j - \varepsilon_a - \varepsilon_b}$$

End a loop

Figure 1. Pseudocode for serial implementation of the GPW-MP2 energy.

functions of all occupied orbitals ($\psi_i(\vec{R})$) are precalculated on real space grids, which speeds up calculation of the pair density ρ^{ia} in the main loop but is not strictly necessary. In the next step, the outer loop iterates over all virtual orbitals a while the inner one loops over occupied orbitals i . For each value of a , the MO ERIs $(ia|jb)$ for all other indices are available after the inner loop, making it possible to compute both Coulomb and exchange contributions to $E^{(2)}$ with $O(o^2v)$ memory usage,

which compares favorably with the $O(on^2)$ memory required in the standard direct canonical algorithm. Other objects, such as the stored grids and molecular orbital coefficients, require memory scaling no worse than quadratic with system size. In the inner loop, all grid operations and integral transformations for a given pair ia are performed. The density $\rho^{ia}(\vec{R})$ on the real space grid is simply obtained by multiplying the values for $\psi_i(\vec{R})$ and $\psi_a(\vec{R})$ and is transformed by FFT to reciprocal space, where the Poisson equation is solved. An inverse FFT yields the potential in real space, which is used in the numerical integration procedure to yield the $(ia|\lambda\sigma)$ integrals. The latter are stored as a sparse matrix, which can directly be employed in the following index transformations that yield the MO ERIs $(ia|jb)$. Note again that the first transformation can exploit the sparsity of the B^{ia} matrix, while the second transformation cannot. The main features of the serial GPW-MP2 algorithm are summarized in Table 1.

3.2. Parallel Algorithm. The parallel algorithm for the GPW-MP2 energy calculation has been designed to enable calculations on large systems and display excellent scalability. This implies that the computational load and amount of data communicated per process decreases linearly as the number of processes (N_p) increases. Furthermore, the computational load is easily balanced, and the communication pattern involves relatively large messages between a small subset of all possible pairs of processes. Additionally, no significant data is fully replicated, and memory usage can be decreased as the number of processes is increased. This is achieved by a multilevel parallelization scheme and a careful process layout. The first level of parallelization corresponds to the work performed for a given ia pair. The second level of parallelization corresponds to a distribution of the nearly independent calculations for each of the ia pairs. The N_p processes are therefore split in N_G groups, each group working on a given ia pair and consisting of N_w processes ($N_p = N_G N_w$). The first level of parallelization is complicated, involving parallel FFTs, halo-exchanges, and sparse matrix multiplications over N_w processes. However, this level is readily available, as it corresponds to the standard parallelization scheme for DFT calculations in CP2K.⁵¹ For example, for the third and fourth quarter transformation, both molecular orbitals and half-transformed integrals are represented as sparse distributed matrices, which can be multiplied using a general purpose parallel sparse matrix multiplication library we recently developed and used extensively in linear scaling calculations.^{58,59} As a rule of thumb, reasonable speed ups are observed as long as $N_w \leq o$, while memory usage benefits from the nearly perfect distribution of the grids and

Table 1. Analysis of the Computational Complexity of the Serial and Parallel GPW-MP2 Energy Algorithms As a Function of the Calculation Parameters^a

	serial		parallel	
	memory	execution time	memory	execution time
wave functions calculation	oS	nS	$(oS/N_i N_w)$	$(o/N_i + v/N_a)S/N_w$
FFT and Poisson solver	S	$ovS \log S$	(S/N_w)	$ovS \log S/N_p$
v^{ia} integration	S	ovn	(S/N_w)	ovn/N_p
first quarter transformation	on	o^2vn	(on/N_w)	o^2vn/N_p
second quarter transformation	ov	o^2v^2n	(ov/N_w)	o^2v^2n/N_p
MP2 energy contraction	o^2v	o^2v^2	$(o^2v/N_i N_w)$	o^2v^2/N_p
Communication			$(o^2v/N_i^2 N_w)$	$(N_i - 1/N_i)(o^2v^2/N_p)$

^a n number of basis functions, o and v number of occupied and virtual orbitals, S grid size, N_i and N_a number of occupied and virtual divisions, N_G and N_w number of groups and group size, N_p number of processes. N_p , N_w , N_G , N_w , and N_p are related by $N_G = N_i N_a$ and $N_p = N_G N_w$.

sparse matrices. Nevertheless, the best performance is obtained if groups do not communicate across nodes, ideally, if memory permits, $N_w = 1$. The second level of parallelization is more straightforward, as it only requires interprocess communications of fully transformed ERIs. In order to distribute the ia pairs efficiently, the occupied orbitals i and the virtual orbitals a are split into N_i and N_a disjoint ranges, respectively. A 2D Cartesian layout with dimensions $N_i \times N_a$ is considered for the N_G groups ($N_G = N_i N_a$) giving each group coordinates (n_i, n_a) and the corresponding index ranges $[i_{start}^{n_i}, i_{end}^{n_i}]$ and $[a_{start}^{n_a}, a_{end}^{n_a}]$. Additionally, each of the N_w processes within a group is given an index n_w , so that a process is uniquely identified by its coordinate triplet (n_i, n_a, n_w) . Finally, the b index is split in N_w ranges $b_{start}^{n_w}, b_{end}^{n_w}$ while a splitting of j is not necessary.

The pseudocode of the parallel algorithm is shown in Figure 2 and it follows the serial algorithm closely (but with restricted

```

Assign each process its coordinate-triplet  $(n_i, n_a, n_w)$ 
Create ranges  $[i_{start}^{n_i}, i_{end}^{n_i}]$ ,  $[a_{start}^{n_a}, a_{end}^{n_a}]$ ,  $[b_{start}^{n_w}, b_{end}^{n_w}]$ 
Loop over  $i$  occupied orbitals ( $i_{start}^{n_i} \leq i \leq i_{end}^{n_i}$ )
    Calculate wavefunction  $\psi_i(\vec{R})$  on the real space grid
    Store  $\psi_i(\vec{R})$ 
End  $i$  Loop
Loop over  $a$  virtual orbitals ( $a_{start}^{n_a} \leq a \leq a_{end}^{n_a}$ )
    Calculate wavefunction  $\psi_a(\vec{R})$  on the real space grid
    Loop over  $i$  occupied orbitals ( $i_{start}^{n_i} \leq i \leq i_{end}^{n_i}$ )
        Compute  $\rho^{ia}(\vec{R}) = \psi_i(\vec{R}) * \psi_a(\vec{R})$  on the real space grid
        Transfer  $\rho^{ia}(\vec{R}) \rightarrow \rho^{ia}(\vec{G})$ :  $\rho^{ia}(\vec{G}) = \text{FFT}[\rho^{ia}(\vec{R})]$ 
        Solve Poisson's Equation:  $\rho^{ia}(\vec{G}) \rightarrow v^{ia}(\vec{G})$ 
        Transfer  $v^{ia}(\vec{G}) \rightarrow v^{ia}(\vec{R})$ :  $v^{ia}(\vec{R}) = \text{FFT}^{-1}[v^{ia}(\vec{G})]$ 
        Integrate Potential in real space:  $(ia|\lambda\sigma) = \mathbf{B}_{\lambda\sigma}^{ia} = \int v^{ia}(\vec{R}) \phi_\lambda(\vec{R}) \phi_\sigma(\vec{R}) d\vec{R}$ 
        Index transformation  $\mathbf{V}^{ia} = \mathbf{C}_\rho^\dagger \mathbf{B}^{ia} \mathbf{C}_v$ 
        Redistribute and store  $\mathbf{V}^{ia}$  (all  $j$ ,  $b_{start}^{n_w} \leq b \leq b_{end}^{n_w}$ )
    End  $i$  Loop
    Loop over  $N_i$  processes with same  $n_a$  and  $n_w$  but different  $n_i$ 
        determine the coordinates  $n_i^S$  and  $n_i^R$  of sending and receiving process.
        Receive  $(ja|ib)$  from  $(n_i^R, n_a, n_w)$ 
             $(i_{start}^{n_i^R} \leq j \leq i_{end}^{n_i^R}, i_{start}^{n_i^S} \leq i \leq i_{end}^{n_i^S}, b_{start}^{n_w} \leq b \leq b_{end}^{n_w})$ 
        Send  $(ia|jb)$  to  $(n_i^S, n_a, n_w)$ 
             $(i_{start}^{n_i^S} \leq j \leq i_{end}^{n_i^S}, i_{start}^{n_i^R} \leq i \leq i_{end}^{n_i^R}, b_{start}^{n_w} \leq b \leq b_{end}^{n_w})$ 
         $E^{(2)} = E^{(2)} + \sum_{i,j,b} \frac{(ia|jb)[2(i|jb) - (j|ib)]}{\epsilon_i + \epsilon_j - \epsilon_a - \epsilon_b}$ 
             $(i_{start}^{n_i^R} \leq j \leq i_{end}^{n_i^R}, i_{start}^{n_i^S} \leq i \leq i_{end}^{n_i^S}, b_{start}^{n_w} \leq b \leq b_{end}^{n_w})$ 
    End loop over processes
End  $a$  loop
Global summation of  $E^{(2)}$ 

```

Figure 2. Pseudocode of the parallel GPW-MP2 energy.

index ranges for i and a) until the end of the inner loop over i . Here, as a last step of the inner loop, the matrix of fully transformed integrals \mathbf{V}^{ia} is redistributed within the group, so that the full range of j and the restricted range of b , corresponding the process' index n_w , is stored locally. After completion of the loop over i the intergroup communication takes place, and here the benefit of the process layout becomes apparent. Indeed, only processes with identical coordinates n_a and n_w need to exchange data, i.e., only within small subgroups of size N_i communication takes place. This is due to the fact that for a given pair ab only $(ia|jb)$ and $(ja|ib)$ need to be

simultaneously available to a process. Since each process stores only ERIs $(ia|jb)$ for i in $[i_{start}^{n_i}, i_{end}^{n_i}]$ and all j , the locally held integrals can be contracted if integrals are received from all other processes that store the ERIs for which $i \notin [i_{start}^{n_i}, i_{end}^{n_i}]$ for the current ab pair. This communication step is easily accomplished by employing the standard message passing interface (MPI) point-to-point communication protocol.⁶⁰ The fact that the computational effort for every ia pair is essentially the same implies that processes arrive well synchronized at the communication step, contributing to the scalability of the algorithm. The size of each message send is $O(v\sigma^2/N_w N_i^2)$, while the number of message exchanges, including the loop over a , is $O((N_i - 1)v/N_a)$, yielding an expected communication time $O((N_i - 1)/N_i)(\sigma^2 v^2/N_p)$ in the bandwidth-limited regime. Note that if only the spin opposite (SO) component of the MP2 energy is required, the MO ERIs do not need to be communicated among processes, yielding an essentially communication-free algorithm with reduced $O(on/N_w)$ memory usage. The main features of the parallel GPW-MP2 algorithm are summarized in Table 1.

4. BENCHMARK CALCULATIONS

4.1. Computational Details. Basis Sets, Thresholds, and Pseudopotentials. The GPW-MP2 method as implemented in CP2K⁵⁰ has been employed for all calculations in this manuscript. The MP2 calculations are based on pseudopotentials of the form suggested by Goedecker, Teter, and Hutter (GTH) in ref 61 but specifically parametrized for Hartree–Fock (HF) calculations. In this way, core states do not need to be represented and valence orbitals are smooth, as required by the GPW method. Valence-only basis sets have been generated for use with these pseudopotentials and are suitable for MP2, i.e., of the correlation-consistent type. The basis sets have been labeled as cc-DZVP, cc-TZVP, and cc-QZVP, denoting increasing quality. The number of primitive Gaussian functions (for the valence only) has been chosen to be 4, 5, and 6 for cc-DZVP, cc-TZVP, and cc-QZVP, respectively. The three primitive Gaussian functions with higher exponent have been used to generate a contracted Gaussian, while the others have been kept uncontracted as in the split valence scheme. For the cc-QZVP basis the most diffuse functions have exponents $H = 0.13906$, $Li = 0.16636$, $C = 0.0597$, $O = 0.10700$. The basis sets have been augmented by the polarization functions taken from the all-electron basis set cc-pVXZ ($X = D, T, Q$) of Dunning^{62,63} up to g-functions. For further details about the basis and pseudopotential parameters we refer to the Supporting Information. Despite the relatively diffuse nature of the Gaussian primitives, our robust implementation of Hartree–Fock exchange^{64,65} allows for stable calculations in the condensed phase.^{65,66} The Schwarz screening threshold for the HF calculations is in the range 10^{-8} – 10^{-10} for the molecular crystals, going down to 10^{-14} for bulk LiH with the most extended basis set. Periodic calculations are based on a truncated Coulomb operator for Hartree–Fock exchange⁶⁵ using approximately one-half the length of the smallest edge of the simulation cell as truncation radius. The threshold for the SCF convergence was 10^{-7} or tighter. The PW cutoff for the HF or DFT part of the calculations was $E_{\text{cut}} = 1200$ Ry to guarantee convergence of the exchange and correlation functional, at small cost compared to the MP2 calculation. The MP2 calculation employed high-quality PW cutoffs of $E_{\text{cut}} = 300$ Ry, $E_{\text{cut}}^{\text{rel}} = 50$ Ry, $\epsilon_{\text{filter}} = 10^{-7}$, and $\epsilon_{\text{grid}} = 10^{-6}$, unless mentioned otherwise. Gas-phase systems have been computed

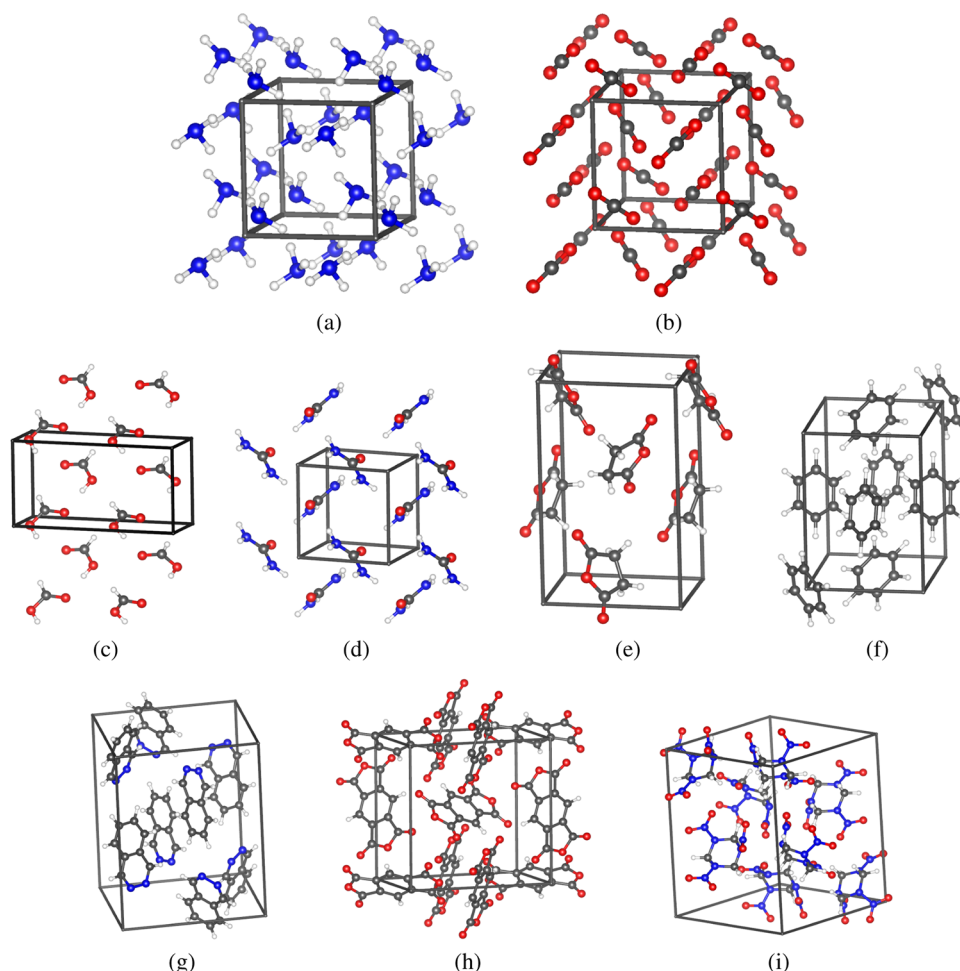


Figure 3. Unit cell and molecules of the supercell for the molecular crystals studied. For all crystals $\alpha = \beta = \gamma = 90^\circ$; all lattice parameters expressed in Angstroms. (a) NH₃, $a = b = c = 5.048$, supercell $2 \times 2 \times 2$, $N_{\text{mol}} = 32$. (b) CO₂, $a = b = c = 5.55$, supercell $2 \times 2 \times 2$, $N_{\text{mol}} = 32$. (c) Formic acid, $a = 10.241$, $b = 3.544$, $c = 5.356$, supercell $1 \times 3 \times 2$ (refcode FORMAC01), $N_{\text{mol}} = 24$. (d) Urea, $a = b = 5.645$, $c = 4.704$, supercell $2 \times 2 \times 2$ (refcode UREAXX09), $N_{\text{mol}} = 16$. (e) Succinic anhydride, $a = 5.4257$, $b = 6.9746$, $c = 11.7167$, supercell $2 \times 2 \times 1$ (refcode SUCANH15), $N_{\text{mol}} = 16$. (f) Benzene, $a = 7.398$, $b = 9.435$, $c = 6.778$, supercell $2 \times 1 \times 2$ (refcode BENZEN07), $N_{\text{mol}} = 16$. (g) 2,3-Diazanaphthalene, $a = 13.695$, $b = 10.557$, $c = 9.285$, supercell $1 \times 1 \times 1$ (refcode DAZNAP), $N_{\text{mol}} = 8$. (h) Pyromellitic dianhydride, $a = b = 10.792$, $c = 7.4128$, supercell $1 \times 1 \times 2$ (refcode PYMDAN), $N_{\text{mol}} = 8$. (i) Trinitro-triazacyclohexane, $a = 13.182$, $b = 11.574$, $c = 10.709$, supercell $1 \times 1 \times 1$ (refcode CTMTNA), $N_{\text{mol}} = 8$.

using cluster boundary conditions for solving the Poisson equation.⁵⁵

Geometries. For all molecular crystals, supercells have been generated by replicating the unit cell, so that the smallest edge was larger than 9 Å, in order for the Γ -point approximation to be reasonable. The geometries of the NH₃ and CO₂ crystals have been built from the experimental lattice parameter and the space group ($a = 5.048$ Å, $P2_13$, for NH₃; $a = 5.55$ Å, $Pa-3$, for CO₂) as detailed in ref 67. The experimental geometries of the other molecular crystals have been retrieved from the Cambridge Structural Database (CSD).⁶⁸ The positions of the hydrogen atoms of these geometries have been further relaxed at the DFT/BLYP^{69,70} level employing the cc-TZVP basis set. The main features of the structure of each crystal, together with the supercell used in the calculation and the CSD refcode, are reported in the caption of Figure 3. The LiH crystal geometry is based on the experimental value of the lattice parameter ($a = 4.084$ Å).

Cohesive Energies and Lattice Parameter Optimization. The counterpoise (CP) corrected cohesive energy per molecule at a given volume V has been computed as

$$E_{\text{coh}}^{\text{CP}}(V) = \frac{E_{\text{supercell}}(V)}{N_{\text{mol}}} - E_{\text{mol}}^{\text{gas}} - E_{\text{mol+ghost}}^{\text{crystal}}(V) + E_{\text{mol}}^{\text{crystal}}(V) \quad (7)$$

Here, N_{mol} is the number of molecules per supercell, $E_{\text{supercell}}(V)$ the total energy of the supercell, and $E_{\text{mol+ghost}}^{\text{crystal}}(V)$, $E_{\text{mol}}^{\text{crystal}}(V)$, and $E_{\text{mol}}^{\text{gas}}$ the total energy of an isolated molecule in either the crystal geometry ($E_{\text{mol+ghost}}^{\text{crystal}}(V)$ and $E_{\text{mol}}^{\text{crystal}}(V)$) or a gas-phase geometry ($E_{\text{mol}}^{\text{gas}}$). $E_{\text{mol+ghost}}^{\text{crystal}}(V)$ includes ghost atoms from the 12 nearest neighbor molecules in the case of NH₃ and CO₂, while only the first coordination shell has been retained for the other molecular crystals. This procedure has also been followed in refs 67 and 71. In the case of LiH, this term has been computed using the fully periodic crystal geometry of the employed supercell. The gas-phase geometry employed for NH₃ and CO₂ corresponds to the one specified in ref 67. The other molecular crystals have been computed twice, once with gas-phase geometries relaxed at the B3LYP/cc-TZVP level^{70,72,73} and once for direct comparison with ref 71, using the crystal geometry also for the gas-phase geometry.

Lattice parameter optimization has been carried out for the NH_3 and CO_2 crystals. The employed procedure is approximate, as MP2 gradients and stresses are currently not available in CP2K, but is similar to the procedure in ref 67. First, structures have been relaxed at a DFT/B3LYP level with the cc-TZVP basis set for various values of the lattice parameter. Next, $E_{\text{coh}}^{\text{CP}}(V)$ has been computed for each of these geometries. Finally, these results have been fitted with a third-order Birch–Murnaghan equation of state in order to get the equilibrium cohesive energy and lattice parameter.

To assess the accuracy of computed cohesive energies, these values have been compared to the experimental sublimation enthalpies ($\Delta H(s)$). However, it has to be emphasized that this comparison includes theoretical bias and is subject to experimental error. Indeed, for nonvolatile compounds, the sublimation enthalpies can be hard to measure and be subject to several kJ/mol error. Experimental sublimation enthalpies usually are obtained at high temperature, while the cohesive energy is a zero-temperature property. Only in a few cases can experimental sublimation enthalpies be extrapolated down to 0 K, CO_2 being such an example:⁷⁴ 26.8 kJ/mol at 0 K, 25.2 kJ/mol at 195 K. Even at 0 K, zero-point energy differences between gas and crystal should be taken into account, and in fact, the anharmonicity of molecular crystals implies that also lattice parameters might need to be corrected for quantum effects to be truly comparable with experiment. Such corrections require calculation of vibrational or phonon properties, see, for example, ref 75 for an early example based on a force field description of molecular crystals, and this has not been attempted in this work.

4.2. GPW-MP2 Accuracy. In order to judge the impact of the PW cutoff (E_{cut}) and the multigrid relative cutoff ($E_{\text{cut}}^{\text{rel}}$) on the accuracy of the GPW-MP2 energy, calculations with various values for these parameters have been performed and are summarized in Figure 4. The benchmark set is based on 10

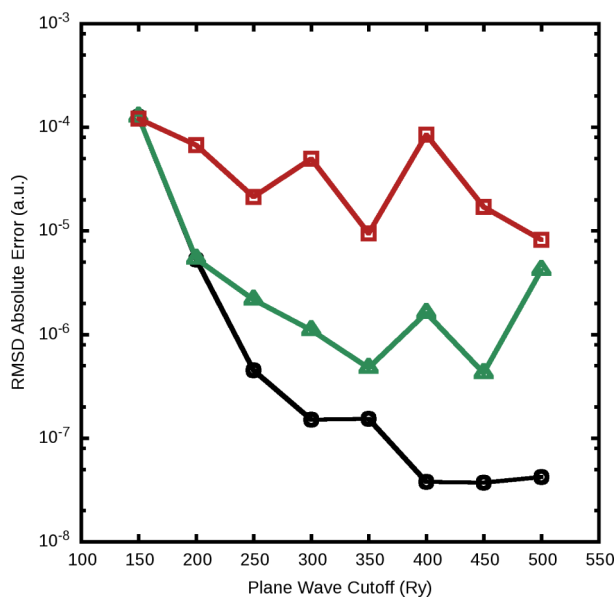


Figure 4. Root-mean-square deviation (rmsd) of the absolute error for the GPW-MP2 energy as a function of the plane wave cutoff (E_{cut}) for different values of the relative cutoff ($E_{\text{cut}}^{\text{rel}}$). Red squares $E_{\text{cut}}^{\text{rel}} = 30$ Ry, green triangles $E_{\text{cut}}^{\text{rel}} = 40$ Ry, and black circles $E_{\text{cut}}^{\text{rel}} = 50$ Ry. Nonmonotonic behavior of the curves is the result of fortuitous cancellation of errors.

molecules (from Figure 3 and H_2O) in the gas phase with the cc-TZVP basis, for which reference energies have been obtained using a traditional direct MP2 algorithm based on analytic four-center integrals over atomic orbitals. The root-mean-square deviation (rmsd) of the absolute difference between the GPW-MP2 energy and the traditional MP2 implementation is used as a measure of the error. Tight values $\epsilon_{\text{filter}} = 10^{-12}$ and $\epsilon_{\text{grid}} = 10^{-12}$ together with a 17 Å cubic cell and cluster boundary conditions have been used to guarantee convergence with respect to these parameters. It can be observed that the GPW-MP2 energy converges rapidly with respect to both parameters E_{cut} and $E_{\text{cut}}^{\text{rel}}$ in particular if one realizes that the time for integration in the MP2-GPW algorithm grows slowly as $E_{\text{cut}}^{3/2}$. Not unexpectedly, both parameters need to be increased simultaneously in order to obtain accurate results. The combinations 300/50, 250/40, and 200/30 Ry yield errors of approximately 10^{-6} , 10^{-5} , and 10^{-4} Hartree, respectively. Note again that E_{cut} depends on the largest exponent in the basis set used, while $E_{\text{cut}}^{\text{rel}}$ is system independent.

4.3. Performance of the Parallel Algorithm. To assess the performance of the parallel algorithm, test calculations on molecular crystals of NH_3 and CO_2 have been performed. For NH_3 a cc-TZVP-quality basis set has been chosen, while CO_2 has been described with a cc-QZVP basis. Each supercell contains 32 molecules, resulting in 2272 and 5184 basis functions, respectively. The speed up and the parallel efficiency for the two test cases are reported in Figure 5. For both benchmarks the algorithm shows very good parallel scalability in a wide range. In particular, in the case of CO_2 , the efficiency remains higher than 80% even for the 102 400 processes run. For the NH_3 calculation, the number of ia pairs (274 560) becomes similar to the number of processes, making an even distribution of the pairs more difficult. Additionally, the overhead of initializing grids and matrices becomes non-negligible, leading to an efficiency of 70%. At full scale out, the MP2 energy calculation required a wall time of 74 and 518 s, respectively.

4.4. System Size Scaling. In order to validate the expected timings for the important parts of the GPW-MP2 algorithm shown in Table 1 we performed calculations on systems of increasing size. The test system is the supercell of NH_3 , containing 32 molecules, with a cc-DZVP basis. This supercell has been replicated in one dimension, yielding an orthorhombic supercell containing up to 128 molecules. The timings, as obtained from runs on 1200 cores, are shown in Figure 6, together with a fit of the form $y = bx^a$. The measured exponents agree very well with the expected values as reported in Table 1, being very close to 3 for the integration and the Poisson solver, 4 for the first and 5 for the last index transformation. In addition to giving information about the scaling behavior, insight about the prefactor can be inferred from the graph. In particular, the last index transformation has a very small prefactor and an extrapolation suggests that it will only dominate for systems containing more than 200 molecules. Note that in an RI-MP2 calculation this term has a larger prefactor, approximately given by the ratio of basis function in the auxiliary and primary basis. For all system sizes tested, the cost is currently dominated by the integration routine, yielding an apparent overall scaling exponent of the GPW-MP2 algorithm of 3.21.

4.5. Solid LiH. The LiH crystal has become a well-studied benchmark system for condensed phase electronic structure calculations. It has favorable characteristics such as a large band

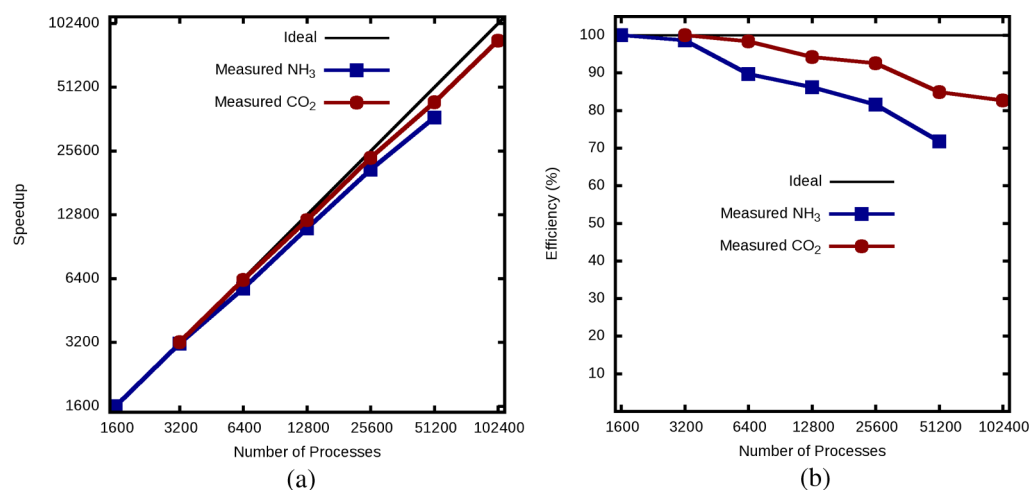


Figure 5. Measured speed up and efficiency for calculation of the GPW-MP2 energy. (a) Speed up measured with respect to 1600 processes for NH₃ crystal and with respect to 3200 processes for CO₂ crystal. (b) Efficiency measured with respect to 1600 processes for NH₃ crystal and with respect to 3200 processes for CO₂ crystal.

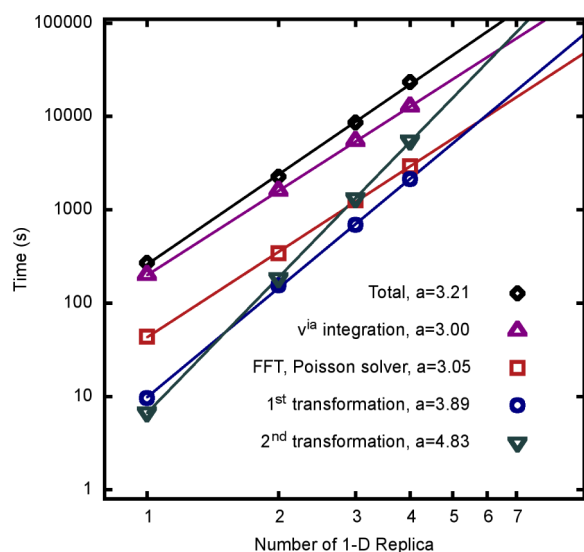


Figure 6. Shown is the time spent in the various significant parts of the GPW-MP2 energy calculation, as a function of the number of replicas of the supercell, containing 32, 64, 96, and 128 molecules of NH₃, respectively. Lines represent a linear two-parameter fit of the form $y = bx^a$. Values of a for each task are reported in the legend.

gap, a simple unit cell, and the absence of heavy elements. This system is thus useful to judge the quality of a method or implementation before more challenging systems, for example, with large unit cells, small band gaps, or complicated chemistry are attempted. Various results for the MP2 contribution to the cohesive energy of LiH have recently been presented in the literature.^{8,76–79} In this section, computation of the MP2 cohesive energy is used to validate the GPW-MP2 method and analyze system size and basis set convergence behavior.

The results obtained for the Hartree–Fock and MP2 contributions to the counterpoise-corrected cohesive energy of LiH are summarized in Table 2. Calculations have been performed up to the $5 \times 5 \times 5$ cell for the cc-DZVP basis, $4 \times 4 \times 4$ for cc-TZVP, and $3 \times 3 \times 3$ for cc-QZVP. MP2 results have been computed for valence-only and all-electron correlation. The largest cells, for each basis, contain roughly 10 000 basis functions, and the $5 \times 5 \times 5$ cell contains 1000 atoms. The

Table 2. Hartree-Fock and MP2 Contributions to the Counterpoise-Corrected Cohesive Energies in mE_h of LiH at the Experimental Geometry for Various Basis Sets and Cell Sizes^a

	$2 \times 2 \times 2$	$3 \times 3 \times 3$	$4 \times 4 \times 4$	$5 \times 5 \times 5$	extr. ($E_X^{n \rightarrow \infty}$)
Hartree–Fock					
cc-DZVP	–139.90	–138.77	–138.37	–138.36	
cc-TZVP	–132.84	–132.20	–132.03	–132.05	
cc-QZVP	–132.60	–132.02			
MP2 all-electron					
cc-DZVP	–29.26	–30.31	–30.58	–30.66	–30.76
cc-TZVP	–38.00	–39.34	–39.68		–39.91
cc-QZVP	–40.55	–41.98	–42.34		–42.59
Extr. ($E_X^{n \rightarrow \infty}$)					–44.09
MP2 valence-only					
cc-DZVP	–27.89	–28.83	–29.06	–29.13	–29.22
cc-TZVP	–36.23	–37.42	–37.73		–37.94
cc-QZVP	–38.68	–39.96	–40.28		–40.51
Extr. ($E_X^{n \rightarrow \infty}$)					–41.93

^aThe text discusses how the extrapolated numbers (italic type) have been obtained.

Hartree–Fock results agree well with previously reported pseudopotential-free calculations performed with CP2K⁶⁶ ($-131.95 mE_h$). The MP2 results depend rather strongly on the basis set and cell size used, and extrapolation is thus necessary. In the following discussion, the MP2 contribution is labeled E_X^n , with X denoting the basis (D,T,Q, ∞) and n the number of repeated unit cells (2,3,4,5, ∞).

As shown in Table 3, the ratio between the cohesive energies for two consecutive cell sizes ($E_X^n/E_X^{(n+1)}$) converges quickly with basis set size. This is equivalent to saying that the system size effect is similar for various basis sets. For example, the difference of (E_X^2/E_X^3) in going from the cc-TZVP to the cc-QZVP basis is around 10^{-4} for both the all-electron and the valence-only case. On the basis of this observation, E_Q^4 is obtained as the extrapolated result ($E_Q^3 \times E_T^4/E_T^3$). Note that the difference between the computed result E_Q^3 and the extrapolated ($E_Q^2 \times E_T^3/E_T^2$) is approximately $4\mu E_h$, validating this approach. In order to estimate the size converged limit, an

Table 3. Ratio between the MP2 Contributions to the Cohesive Energy of LiH for Two Consecutive Cell Sizes ($E_X^n/E_X^{(n+1)}$) with $X = D, T, Q$

	MP2 all electron			MP2 valence only		
	E_X^2/E_X^3	E_X^3/E_X^4	E_X^4/E_X^5	E_X^2/E_X^3	E_X^3/E_X^4	E_X^4/E_X^5
cc-DZVP	0.9654	0.9911	0.9974	0.9674	0.9921	0.9975
cc-TZVP	0.9661	0.9914		0.9680	0.9920	
cc-QZVP	0.9660			0.9679		

extrapolation for the cell size going to infinity ($E_X^{n \rightarrow \infty}$), for a given basis set, has been performed by a linear fit of the equation $E_X^n = E_X^{n \rightarrow \infty} + S(n \times a)^{-3}$, where n is the number of repeated unit cells and a the lattice constant. The choice of exponent (-3) is justified by the fact that the long-range behavior of the MP2 pair energy follows the London law C_6/d_{ij}^6 , with d_{ij} being the distance between the center of two

distributions,¹⁹ and by integrating over all pairs in the crystal for which $d_{ij} \geq d$. Finally, the size-extrapolated results for each of the basis sets are extrapolated to the basis set limit. This basis set extrapolation is based on the cubic interpolation formula⁸⁰ $E_X^{n \rightarrow \infty} = E_{X \rightarrow \infty}^n + AX^{-3}$ ($X = 2, 3, 4$ for cc-DZVP, cc-TZVP, and cc-QZVP, respectively). The fits are shown in Figure 7 and the extrapolated values reported in Table 2. We note that the extrapolation for the cell size going to infinity yields an asymptotic standard error of the order of few μE_h , but for the basis set extrapolation the estimated error is on the order of one-tenth of mE_h . Finally, the MP2 contribution to the cohesive energy of LiH is estimated to be $-44.09 mE_h$ in the all-electron case and $-41.93 mE_h$ for valence-only correlation.

As summarized in Table 4, the estimates presented in this work are in good agreement with other values reported in the literature. For the all-electron case, excellent agreement with the result reported by Marsman and co-workers⁸ is observed,

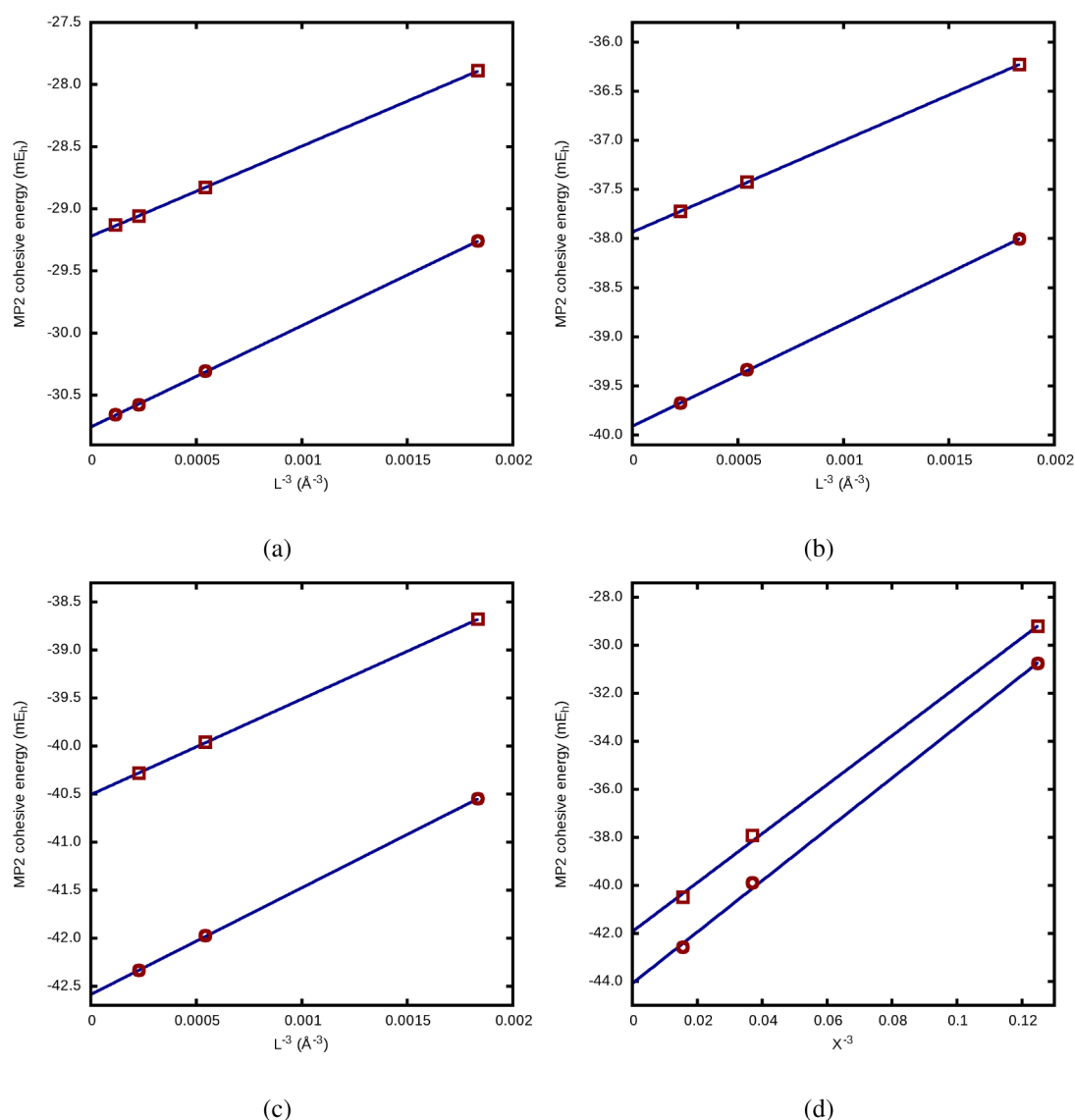


Figure 7. Convergence of the all-electron (circles) and valence-only (squares) MP2 contribution to the cohesive energy of LiH with respect to the cell size and basis set. L is the length of the cell edge ($L = n \times a$), and $X = 2, 3$, and 4 for cc-DZVP, cc-TZVP, and cc-QZVP, respectively. (a) Extrapolation with respect to the cell size for the cc-DZVP basis set. (b) Extrapolation with respect to the cell size for the cc-TZVP basis set. (c) Extrapolation with respect to the cell size for the cc-QZVP basis set. (d) Extrapolation with respect to the basis set for the size-converged MP2 cohesive energy.

Table 4. Comparison of the Basis Set Limit Estimation of the MP2 Contribution to the Cohesive Energy of LiH at the Experimental Geometry ($a = 4.084 \text{ \AA}$). All energies in mE_h ^a

code/method		$E_{\text{coh}}^{\text{MP2}}$
hierarchical method ^b	all-electron	−43.43
VASP ^c	all-electron	−43.99
CP2K ^d	all-electron	−44.09
CRYSCOR ^e	valence-only	−41.34
incremental scheme ^f	valence-only	−41.55
CP2K ^d	valence-only	−41.93

^aResults calculated with different approaches, reported by different authors. ^bNolan and co-workers.⁷⁸ ^cMarsman and co-workers.⁸ ^dThis work. ^eUsvyat and co-workers.⁷⁷ ^fStoll and co-workers.⁷⁶

the deviation is only $0.1 mE_h$. The other values show larger discrepancies, up to 0.6 millihartree. We believe that these differences are due to the delicate nature of the basis set extrapolation. In the condensed phase, a robust extrapolation procedure might be easier to establish for a plane waves basis, and a detailed analysis for such an approach has recently been presented in ref 79. Without extrapolation and for very similar basis sets, better agreement is observed. For example, the value of the valence-only MP2 energy reported by Stoll and co-workers⁷⁶ at the triple- ζ level is $-38.02 mE_h$, very close to the $-37.94 mE_h$ obtained with the cc-TZVP basis. With the “basis set A” proposed by Usvyat and co-workers⁷⁷ (with small adaptations of the core–valence part of the basis to the pseudopotentials), we find $-38.97 mE_h$ for the valence-only contribution, in good agreement with $-39.08 mE_h$ reported in ref 77.

4.6. NH_3 and CO_2 Molecular Crystals. The molecular crystals of NH_3 and CO_2 present two useful benchmark systems, as they differ in the nature of their interaction: NH_3 is hydrogen bonded, while CO_2 is not. Furthermore, results for these systems can be compared to results presented in ref 67 and obtained by LMP2 as implemented in CRYSCOR. The effects of the basis set and supercell size on the cohesive energy at the experimental geometry are reported in Table 5. Not unexpectedly, it can be seen that cc-DZVP yields poor results for the cohesive energy, and a cc-TZVP basis is required to yield a cohesive energy within approximately 5 kJ/mol of the basis set extrapolated result. However, the smaller cc-DZVP basis allows for larger systems and hence can be used to study

Table 5. Counterpoise-Corrected Cohesive Energy ($E_{\text{coh}}^{\text{CP}}$ in kJ/mol) for the NH_3 and CO_2 Crystals^a

	NH_3		CO_2	
	HF	HF+MP2	HF	HF+MP2
cc-DZVP	−8.43	−25.78 (−22.6)	−7.48	−8.92 (−8.9)
cc-DZVP ^b	−8.80	−27.89	−7.47	−11.46
cc-TZVP	−5.98	−30.93 (−29.6)	−5.86	−20.95 (−19.3)
cc-QZVP	−5.60	−32.76 (−32.3)	−5.91	−23.28 (−24.4)
extrapolated ^c	−5.52	−33.93	−5.99	−26.09
experiment ^d		−36.3		−31.1

^aResults have been calculated employing different basis sets and system sizes at the experimental geometry. Values in parentheses refer to the HF+LMP2 results from ref 67 as obtained with the CRYSCOR program using basis sets of comparable quality. ^bCalculation performed with supercell $3 \times 3 \times 3$ instead of $2 \times 2 \times 2$. ^c(T–Q) extrapolation toward the basis set limit.⁸⁰ ^dValues from ref 67. See also ref 81 for NH_3 and refs 82 and 83 for CO_2 .

the size dependence of the result. Indeed, since our results are obtained at the Γ -point only, the size of the supercell matters. Fortunately, we see that the difference between the cohesive energies obtained $2 \times 2 \times 2$ and $3 \times 3 \times 3$ unit cells (32 and 108 molecules, respectively) is rather small, a few kJ/mol , smaller than the difference between cc-TZVP and basis set-extrapolated results. Note that the HF results are less sensitive to both system size and basis set effects. Of course, the Hartree–Fock level of theory is a poor description for these systems, since the MP2 correlation contributes almost 80% of the cohesive energy. Careful estimates of the MP2 cohesive energy could combine the size effect as computed with smaller basis sets with basis set extrapolated results for smaller supercells, as we illustrated for LiH. Furthermore, our results are in good agreement with those reported in ref 67 despite the various differences in methodology, such as the use of pseudopotentials, corresponding basis sets, local MP2, etc. Lattice parameters are within 0.1 \AA of the HF+LMP2 results and of experiment.

In Figure 8, lattice parameter optimization curves are reported as obtained at various levels of theory. In the case of NH_3 , the quality of the pseudopotential approximation has been verified as illustrated by the excellent agreement between the HF results as obtained with pseudopotentials and the corresponding cc-TVZP basis and an all-electron calculation employing the Dunning cc-pVTZ basis. For both NH_3 and CO_2 , the DFT/B3LYP and HF results predict an equilibrium lattice parameter much larger than the experimental one and a cohesive energy that is far from the experimental one. The HF results are significantly improved by the MP2 correction, and the same can be said for the dispersion corrections in the case of B3LYP. The calculated equilibrium values of a and E_{coh} are summarized in Table 6. The MP2 lattice constants are within approximately 1% of the experimental results, and while the same holds for B3LYP-D3,⁸⁴ a larger error is observed with B3LYP-D2.⁸⁵ The cc-TZVP and cc-QZVP MP2 results are very similar, suggesting that the former might be a cost-effective choice for these calculations.

4.7. Cohesive Energy of Molecular Crystals from MP2 and Double-Hybrid DFT. Finally, cohesive energies for the remaining molecular crystals reported in Figure 3 are presented in Table 7, in all cases using the experimental crystal cell and employing the cc-TZVP basis. Here, a wider set of theoretical methods is employed, including MP2 as well as double-hybrid functionals. These values are compared to the experimentally measured sublimation enthalpies, with the caveats mentioned above. The rmsd, measured over this relatively small test set, is reported as well. First, HF and DFT/B3LYP methods display the largest rmsd, demonstrating that these methods are not suitable for computing, even to a qualitative level, the lattice energy of molecular crystals. Small molecules that interact mostly via hydrogen bonds and dipole–dipole electrostatics are described best, but van der Waals dominated complexes can have even a negative computed lattice energy. On the other hand, the D2 and D3 dispersion corrections appreciably improve the bare B3LYP results; for all cases the computed lattice energy goes closer to the experimental value, decreasing significantly the rmsd. However, both B3LYP-D2 and B3LYP-D3 tend to overbind the crystals, B3LYP-D3 being slightly worse. With an rmsd of 16.9 kJ/mol , the lattice energies calculated at the MP2 level outperform the DFT results. The molecules that display the largest deviations, benzene and pyromellitic dianhydride, have a large π electronic delocaliza-

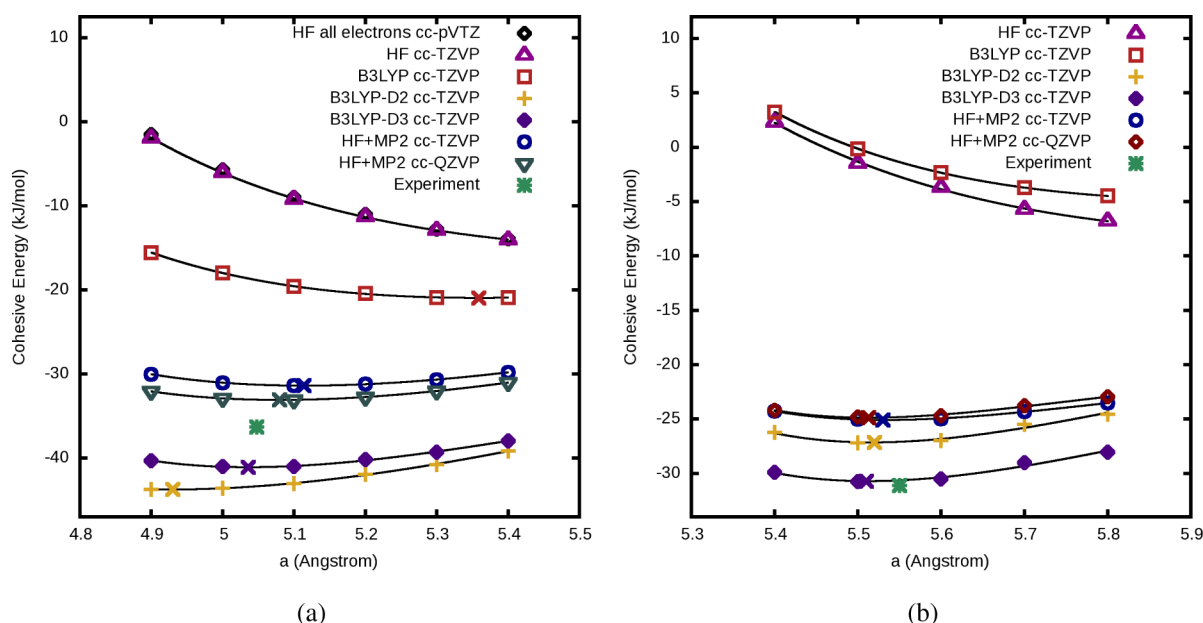


Figure 8. Lattice parameter optimization curves for NH_3 (a) and CO_2 (b) computed at different levels of theory and different basis sets. Crosses represent the location of the minimum point for each curve.

Table 6. Equilibrium Counterpoise-Corrected Cohesive Energy ($E_{\text{coh}}^{\text{CP}}$ in kJ/mol per molecule) and Lattice Parameter (a , in Angstroms) for the NH_3 and CO_2 Crystals Calculated Employing Different Methods^a

	NH_3		CO_2	
	a	E_{coh}	a	E_{coh}
HF	5.98	−15.7	6.05	−5.00
B3LYP	5.36	−20.9	6.20	−8.20
B3LYP-D2	4.93	−43.7	5.52	−27.2
B3LYP-D3	5.04	−41.1	5.51	−30.7
HF+MP2	5.11	−31.4	5.53	−25.1
HF+MP2 ^b	5.08	−33.1	5.51	−24.9
HF+LMP2 ^c	5.02	−36.6	5.59	−26.6
Exp.	5.048	−36.3	5.55	−31.1

^aThe basis set is cc-TZVP, except when specified otherwise.

^bCalculated with the cc-QZVP basis set. ^cReference 67 calculated with the aug(d,f)-TZPP basis set.

tion, which is known to be unfavorable for the performance of MP2. Relaxation of the gas-phase geometry has a large effect on the cohesive energies for those systems with strong interactions in the crystal and is only negligible for benzene. Also in this case there is good agreement between the computed GPW-MP2 energies (nonrelaxed case) and the LMP2 calculations reported in ref 71.

The spin component scaled variants of the MP2 method tend to improve slightly over the performance of standard MP2, the MP2-SCS method of Grimme⁸⁶ yielding the smallest rmsd. This is largely due to the better agreement observed for pyromellitic dianhydride, for which the discrepancy is reduced from ~40 to ~20 kJ/mol. Interestingly, the MP2-SCS(MI) of Distasio et al.,⁸⁸ which has been parametrized explicitly for molecular interactions using the S22 database⁹⁰ as training set, does not perform best for the molecular interactions in these crystals. It is the best method for benzene, which is also present in the S22 database in a similar configuration as the one found in the crystal, but it is less accurate for formic acid, which is

present in S22 in a fairly different geometry. This suggests that a database of accurate cohesive energies for molecular crystals would complement the S22 set by providing a wider range of molecular geometries and thus provide valuable input for development of improved methods.

Two different double-hybrid functionals have been tested: B2PLYP and DSD-BLYP with and without dispersion corrections.¹¹ The main difference between these two functionals is that the MP2-like term is scaled with a single parameter in B2PLYP, while independent parameters are used for the same spin and opposite spin MP2-like terms in DSD-BLYP, as is done in MP2-SCS. B2PLYP without dispersion correction shows a large rmsd. B2PLYP-D3, with an added D3 correction, improves slightly over MP2. Finally, the DSD-BLYP functional yields the best results for pyromellitic dianhydride, which is the source of large errors for other methods. Surprisingly, adding the D3 correction to DSD-BLYP actually increases the rmsd, increasing the errors for some compounds significantly.

5. CONCLUSIONS

In the present work, a novel method for calculation of the canonical MP2 energy of finite and extended systems has been presented. The crucial aspect of the method is that half-transformed electron repulsion integrals (ERIs) ($ial\sigma$) are directly calculated. This is possible using a mixed Gaussian and plane wave approach, which allows for computing the electrostatic potential v^{ia} of the occupied-virtual pair density ρ^{ia} in an auxiliary basis and numerically integrating over products of basis functions $\lambda\sigma$. The method is naturally suited and robust for periodic systems, and numerical accuracy can be easily controlled. The corresponding algorithm shows excellent parallel performance up to 100 000 processes and allows for MP2 calculations of systems containing hundreds of atoms and thousands of basis functions in minutes. Benchmark calculations on solid LiH and molecular crystals have been performed to validate the GPW-MP2 method, and good agreement with literature results and, for most benchmarks,

Table 7. Counterpoise-Corrected Cohesive Energy ($-E_{\text{coh}}^{\text{CP}}$, in kJ/mol) for Molecular Crystals^a

	B	FA	SA	D	PD	U	CT	rmsd
Exp $\Delta H(s)^b$	45	68	81	83	83	92	112	
LMP2 (C) ^c	56.6	63.2	87.0			108.6		
GPW-MP2 (C)	58.7	64.9	84.9	93.3	127.3	106.6	126.6	19.7
GPW-MP2	58.8	55.5	81.2	79.7	123.4	94.6	113.7	16.9
HF	−21.2	26.3	38.6	−5.7	31.3	55.8	49.8	58.1
B3LYP	−12.5	34.1	27.5	−7.0	15.8	64.2	17.3	65.1
B3LYP-D2	56.9	69.1	91.8	84.0	122.0	110.5	128.4	18.5
B3LYP-D3	60.5	71.9	94.7	87.3	128.1	111.6	131.0	21.5
B2PLYP ^d	14.7	44.8	51.0	74.2	60.0	78.4	58.8	29.2
B2PLYP-D3 ^d	53.4	64.7	86.4	77.3	119.8	103.7	119.9	15.6
DSD-BLYP ^d	31.6	54.4	67.6	50.6	88.8	90.9	90.8	17.2
DSD-BLYP-D3 ^d	56.9	67.4	90.8	82.8	128.1	107.4	130.9	20.2
MP2-SCS ^e	38.6	52.2	75.6	62.3	106.4	89.2	112.0	13.6
MP2-SOS ^f	28.5	50.6	72.9	53.6	97.9	86.7	111.2	15.8
MP2-SCS(MI) ^g	47.9	47.3	70.1	63.9	104.6	84.8	90.2	16.5
MP2-SCSN ^h	52.3	44.9	67.1	64.3	103.4	82.3	79.3	19.7

^aB = Benzene (Figure 3f), FA = formic acid (Figure 3c), SA = succinic anhydride (Figure 3e), D = 2,3-diazanaphthalene (Figure 3g), PD = pyromellitic dianhydride (Figure 3h), U = urea (Figure 3d), CT = cyclotrimethylene-trinitramine (Figure 3i). The sign of $E_{\text{coh}}^{\text{CP}}$ has been changed in order to be compared with the experimental sublimation enthalpies $\Delta H(s)$. (C) means that the gas phase geometry has not been relaxed but was constrained to the crystal geometry. ^bTaken from the Supporting Information of ref 71; see also <http://webbook.nist.gov/chemistry/>. ^cLocal MP2 calculation performed with the CRYSCOR program reported from ref 71. ^dThe parameter for these double-hybrid functionals and their relative D3 corrections have been taken from ref 11. ^eSpin component scaled (SCS)⁸⁶ ($p_S = 1.2$, $p_T = 0.333$). ^fScaled opposite spin (SOS)⁸⁷ ($p_S = 1.3$, $p_T = 0$). ^gSpin component scaled (molecular interaction) (SCS(MI))⁸⁸ ($p_S = 0.4$, $p_T = 1.29$). ^hSpin component scaled for nucleobases (SCSN)⁸⁹ ($p_S = 0$, $p_T = 1.76$).

with experiment is obtained. These calculations also suggest that a database with reliable reference cohesive energies for molecular crystals could complement existing gas-phase databases and contribute to development of improved methods and functionals for weak interactions. We believe that the GPW-MP2 method can now be used to study condensed phase systems with a few hundred atoms per unit cell, including not only crystals but also systems without symmetry such as molecules on surfaces and liquids. Advanced techniques, such as RI-MP2 and local MP2, and adaptation to new hardware, such as accelerators, are likely to further improve upon the method presented here.

■ ASSOCIATED CONTENT

Supporting Information

Pseudopotentials and basis-set parameters used in this work. This material is available free of charge via the Internet at <http://pubs.acs.org>.

■ AUTHOR INFORMATION

Corresponding Author

*E-mail: delben@pci.uzh.ch (M.D.B.); hutter@pci.uzh.ch (J.H.); Joost.VandeVondele@mat.ethz.ch (J.V.).

Notes

The authors declare no competing financial interest.

■ ACKNOWLEDGMENTS

We thank Ruyman Reyes Castro and Iain Bethune from the EPCC, UK, supported by PRACE project PA0723, for application analysis and optimization. J.V. acknowledges financial support by the European Union FP7 in the form of an ERC Starting Grant under contract no. 277910. Calculations were enabled by 2011 INCITE awards on the CRAY XK6 using resources of the National Center for Computational Sciences at Oak Ridge National Laboratory (ORNL), which is supported

by the Office of Science of the U.S. DOE under Contract No. DE-AC05-00OR22725, and by the Swiss National Supercomputer Centre (CSCS). The research leading to these results has received funding from the Swiss University Conference through the High Performance and High Productivity Computing (HP2C) Programme.

■ REFERENCES

- (1) Möller, C.; Plesset, M. S. *Phys. Rev.* **1934**, *46*, 618–622.
- (2) Szabo, A.; Ostlund, N. S. *Modern Quantum Chemistry*; McGraw Hill: New York, 1982; pp 350–353.
- (3) Sun, J.-Q.; Bartlett, R. J. *J. Chem. Phys.* **1996**, *104*, 8553–8565.
- (4) Katouda, M.; Nagase, S. *J. Chem. Phys.* **2010**, *133*, 184103.
- (5) Izmaylov, A. F.; Scuseria, G. E. *Phys. Chem. Chem. Phys.* **2008**, *10*, 3421.
- (6) Ayala, P. Y.; Kudin, K. N.; Scuseria, G. E. *J. Chem. Phys.* **2001**, *115*, 9698–9707.
- (7) Pisani, C.; Busso, M.; Capecchi, G.; Casassa, S.; Dovesi, R.; Maschio, L.; Zicovich-Wilson, C.; Schütz, M. *J. Chem. Phys.* **2005**, *122*, 094113.
- (8) Marsman, M.; Gruneis, A.; Paier, J.; Kresse, G. *J. Chem. Phys.* **2009**, *130*, 184103.
- (9) Gruneis, A.; Marsman, M.; Kresse, G. *J. Chem. Phys.* **2010**, *133*, 074107.
- (10) Grimme, S. *J. Chem. Phys.* **2006**, *124*, 034108.
- (11) Goerigk, L.; Grimme, S. *J. Chem. Theory Comput.* **2011**, *7*, 291–309.
- (12) Cremer, D. *WIREs Comput. Mol. Sci.* **2011**, *1*, 509–530.
- (13) Saebø, S.; Pulay, P. *Annu. Rev. Phys. Chem.* **1993**, *44*, 213–236.
- (14) Pulay, P.; Saebø, S. *Theor. Chim. Acta* **1986**, *69*, 357–368.
- (15) Rauhut, G.; Pulay, P.; Werner, H.-J. *J. Comput. Chem.* **1998**, *19*, 1241–1254.
- (16) Schütz, M.; Hetzer, G.; Werner, H.-J. *J. Chem. Phys.* **1999**, *111*, 5691–5705.
- (17) Hetzer, G.; Schütz, M.; Stoll, H.; Werner, H.-J. *J. Chem. Phys.* **2000**, *113*, 9443–9455.
- (18) Saebø, S.; Pulay, P. *J. Chem. Phys.* **2001**, *115*, 3975–3983.

- (19) Pisani, C.; Maschio, L.; Casassa, S.; Halo, M.; Schütz, M.; Usvyat, D. *J. Comput. Chem.* **2008**, *29*, 2113–2124.
- (20) Maslen, P. *Chem. Phys. Lett.* **1998**, *283*, 102–108.
- (21) Maslen, P. E.; Head-Gordon, M. *J. Chem. Phys.* **1998**, *109*, 7093–7099.
- (22) Almlöf, J. *Chem. Phys. Lett.* **1991**, *181*, 319–320.
- (23) Häser, M.; Almlöf, J. *J. Chem. Phys.* **1992**, *96*, 489–494.
- (24) Häser, M. *Theor. Chim. Acta* **1993**, *87*, 147–173.
- (25) Ayala, P. Y.; Scuseria, G. E. *J. Chem. Phys.* **1999**, *110*, 3660–3671.
- (26) Lambrecht, D. S.; Doser, B.; Ochsenfeld, C. *J. Chem. Phys.* **2005**, *123*, 184102.
- (27) Doser, B.; Lambrecht, D. S.; Kussmann, J.; Ochsenfeld, C. *J. Chem. Phys.* **2009**, *130*, 064107.
- (28) Feyereisen, M.; Fitzgerald, G.; Komornicki, A. *Chem. Phys. Lett.* **1993**, *208*, 359–363.
- (29) Weigend, F. *Chem. Phys. Lett.* **1998**, *294*, 143–152.
- (30) Bernholdt, D. E.; Harrison, R. J. *J. Chem. Phys.* **1998**, *109*, 1593–1600.
- (31) Werner, H.-J.; Manby, F. R.; Knowles, P. J. *J. Chem. Phys.* **2003**, *118*, 8149–8160.
- (32) Maschio, L.; Usvyat, D.; Manby, F. R.; Casassa, S.; Pisani, C.; Schütz, M. *Phys. Rev. B* **2007**, *76*, 075101.
- (33) Usvyat, D.; Maschio, L.; Manby, F. R.; Casassa, S.; Schütz, M.; Pisani, C. *Phys. Rev. B* **2007**, *76*, 075102.
- (34) Klopper, W.; Manby, F. R.; Ten-No, S.; Valeev, E. F. *Int. Rev. Phys. Chem.* **2006**, *25*, 427–468.
- (35) Limaye, A. C.; Gadre, S. R. *J. Chem. Phys.* **1994**, *100*, 1303–1307.
- (36) Marquez, A. M.; Dupuis, M. *J. Comput. Chem.* **1995**, *16*, 395–404.
- (37) Nielsen, I. M. B.; Seidl, E. T. *J. Comput. Chem.* **1995**, *16*, 1301–1313.
- (38) Baker, J.; Pulay, P. *J. Comput. Chem.* **2002**, *23*, 1150–1156.
- (39) Ishimura, K.; Pulay, P.; Nagase, S. *J. Comput. Chem.* **2006**, *27*, 407–413.
- (40) Katouda, M.; Nagase, S. *Int. J. Quantum Chem.* **2009**, *109*, 2121–2130.
- (41) Doser, B.; Lambrecht, D. S.; Ochsenfeld, C. *Phys. Chem. Chem. Phys.* **2008**, *10*, 3335.
- (42) Valeev, E. F.; Janssen, C. L. *J. Chem. Phys.* **2004**, *121*, 1214–1227.
- (43) Nakao, Y.; Hirao, K. *J. Chem. Phys.* **2004**, *120*, 6375–6380.
- (44) Nielsen, I. M. B.; Janssen, C. L. *J. Chem. Theory Comput.* **2007**, *3*, 71–79.
- (45) Maschio, L. *J. Chem. Theory Comput.* **2011**, *7*, 2818–2830.
- (46) Lippert, G.; Hutter, J.; Parrinello, M. *Mol. Phys.* **1997**, *92*, 477–488.
- (47) Martinez, T. J.; Carter, E. A. *J. Chem. Phys.* **1994**, *100*, 3631–3638.
- (48) Ishimura, K.; Ten-no, S. *Theor. Chem. Acc.* **2011**, *130*, 317–321.
- (49) Hirata, S.; Iwata, S. *J. Chem. Phys.* **1998**, *109*, 4147–4155.
- (50) The CP2K developers group, CP2K is freely available from: <http://www.cp2k.org/>, 2012.
- (51) VandeVondele, J.; Krack, M.; Mohamed, F.; Parrinello, M.; Chassaing, T.; Hutter, J. *Comput. Phys. Commun.* **2005**, *167*, 103–128.
- (52) Aissing, G.; Monkhorst, H. J. *Int. J. Quantum Chem.* **1993**, *48*, 81–89.
- (53) Martyna, G. J.; Tuckerman, M. E. *J. Chem. Phys.* **1999**, *110*, 2810–2821.
- (54) Blöchl, P. E. *J. Chem. Phys.* **1995**, *103*, 7422–7428.
- (55) Genovese, L.; Deutsch, T.; Neelov, A.; Goedecker, S.; Beylkin, G. *J. Chem. Phys.* **2006**, *125*, 074105.
- (56) Lippert, G.; Hutter, J.; Parrinello, M. *Theor. Chem. Acc.* **1999**, *103*, 124–140.
- (57) Krack, M.; Parrinello, M. *Phys. Chem. Chem. Phys.* **2000**, *2*, 2105–2112.
- (58) VandeVondele, J.; Borstnik, U.; Hutter, J. *J. Chem. Theory Comput.* **2012**, ASAP, DOI: 10.1021/ct200897x.
- (59) Manuscript in preparation, 2012.
- (60) MPI, Message Passing Interface, <http://www.mpi-forum.org/>, 2012.
- (61) Goedecker, S.; Teter, M.; Hutter, J. *Phys. Rev. B* **1996**, *54*, 1703–1710.
- (62) Dunning, T. H. *J. Chem. Phys.* **1989**, *90*, 1007–1023.
- (63) Woon, D. E.; Dunning, T. H. *J. Chem. Phys.* **1993**, *98*, 1358–1371.
- (64) Guidon, M.; Schiffmann, F.; Hutter, J.; VandeVondele, J. *J. Chem. Phys.* **2008**, *128*, 214104.
- (65) Guidon, M.; Hutter, J.; VandeVondele, J. *J. Chem. Theory Comput.* **2009**, *5*, 3010–3021.
- (66) Paier, J.; Diaconu, C. V.; Scuseria, G. E.; Guidon, M.; VandeVondele, J.; Hutter, J. *Phys. Rev. B* **2009**, *80*, 174114.
- (67) Maschio, L.; Usvyat, D.; Schütz, M.; Civalleri, B. *J. Chem. Phys.* **2010**, *132*, 134706.
- (68) Allen, F. H. *Acta Crystallogr., Sect. B: Struct. Sci* **2002**, *58*, 380–388.
- (69) Becke, A. D. *Phys. Rev. A* **1988**, *38*, 3098–3100.
- (70) Lee, C.; Yang, W.; Parr, R. G. *Phys. Rev. B* **1988**, *37*, 785–789.
- (71) Maschio, L.; Civalleri, B.; Ugliengo, P.; Gavezotti, A. *J. Phys. Chem. A* **2011**, *115*, 11179–11186.
- (72) Becke, A. D. *J. Chem. Phys.* **1993**, *98*, 5648–5652.
- (73) Vosko, S. H.; Wilk, L.; Nusair, M. *Can. J. Phys.* **1980**, *58*, 1200–1211.
- (74) Trusler, J. P. M. *J. Phys. Chem. Ref. Data* **2011**, *40*, 043105.
- (75) Warshel, A.; Lifson, S. *J. Chem. Phys.* **1970**, *53*, 582–594.
- (76) Stoll, H.; Doll, K. *J. Chem. Phys.* **2012**, *136*, 074106.
- (77) Usvyat, D.; Civalleri, B.; Maschio, L.; Dovesi, R.; Pisani, C.; Schütz, M. *J. Chem. Phys.* **2011**, *134*, 214105.
- (78) Nolan, S. J.; Gillan, M. J.; Alfè, D.; Allan, N. L.; Manby, F. R. *Phys. Rev. B* **2009**, *80*, 165109.
- (79) Shepherd, J. J.; Grueneis, A.; Booth, G. H.; Kresse, G.; Alavi, A. *Phys. Rev. B* **2012**, *86*, 035111.
- (80) Halkier, A.; Helgaker, T.; Jørgensen, P.; Klopper, W.; Koch, H.; Olsen, J.; Wilson, A. K. *Chem. Phys. Lett.* **1998**, *286*, 243–252.
- (81) Shipman, L. L.; Burgess, A. W.; Scheraga, H. A. *J. Phys. Chem.* **1976**, *80*, 52–54.
- (82) Keesom, W.; Kohler, J. *Physica* **1934**, *1*, 655–658.
- (83) Curzon, A. *Physica* **1972**, *59*, 733.
- (84) Grimme, S.; Antony, J.; Ehrlich, S.; Krieg, H. *J. Chem. Phys.* **2010**, *132*, 154104.
- (85) Grimme, S. *J. Comput. Chem.* **2006**, *27*, 1787–1799.
- (86) Grimme, S. *J. Chem. Phys.* **2003**, *118*, 9095–9102.
- (87) Jung, Y.; Lochan, R. C.; Dutoi, A. D.; Head-Gordon, M. *J. Chem. Phys.* **2004**, *121*, 9793–9802.
- (88) Distasio JR., R. A.; Head-Gordon, M. *Mol. Phys.* **2007**, *105*, 1073–1083.
- (89) Hill, J. G.; Platts, J. A. *J. Chem. Theory Comput.* **2007**, *3*, 80–85.
- (90) Jurecka, P.; Sponer, J.; Cerny, J.; Hobza, P. *Phys. Chem. Chem. Phys.* **2006**, *8*, 1985–1993.